Mater Renew Sustain Energy (2013) 2:16
DOI 10.1007/s40243-013-0016-z

ORIGINAL PAPER

Synthesis of nanosized MnO_2 prepared by the polyol method and its application in high power supercapacitors

E. Goikolea · B. Daffos · P. L. Taberna · P. Simon

Received: 21 May 2013 / Accepted: 11 July 2013 / Published online: 25 July 2013

Abstract Over the last years, the different polymorphs of MnO_2 have been intensely studied as alternative compounds to amorphous hydrous RuO_2 as supercapacitor electrode materials. In the present work, nanosized birnessite-type MnO_2 platelets were synthesized via the polyol method followed by a subsequent ligand removal with NaOH. The resulting compound is easily dispersible in polar solvents, thus allowing the preparation of stable dispersions (2–3 days) that could be used in thin electrode preparation. The capacitance of the synthesized product was 130 F g^{-1} in a potential window of 0.8 V at a scan rate of 2 mV s^{-1}. The synthesized material was also studied using a cavity microelectrode to evaluate the electrochemical performance of the nanostructured oxide at high scan rates. Cyclic voltammetry measurements were successfully carried out both in the previous potential window between 0.1 and 0.9 V (vs. SHE) and in a larger potential window between −0.6 and 1.1 V (vs. SHE) from 0.1 and up to 1,000 mV s^{-1}. Therefore, herein prepared material could be potentially used for high power applications, although further work should be carried out to upscale such compound without compromising the performance.

Keywords Electrochemical capacitors · Pseudocapacitance · Manganese dioxide · Nanostructured materials · Cavity microelectrode

E. Goikolea
CIC Energigune, Arabako Parke Teknologikoa,
Albert Einstein 48, 01510 Miñano, Spain

E. Goikolea · B. Daffos · P. L. Taberna · P. Simon (✉)
Université Paul Sabatier, CIRIMAT UMR CNRS 5085,
31062 Toulouse Cedex 4, France
e-mail: simon@chimie.ups-tlse.fr

Introduction

Now that our energy consumption and production culture is changing toward a more sustainable model, the development of improved energy storage systems (EESs) is essential for the consolidation of the different renewable energy sources. For all those applications where high power is a requirement, small electrical devices such as screwdrivers or camera flashes and acceleration/braking units in electric vehicles for instance, supercapacitors or electrochemical capacitors have emerged as a promising type of EES [1, 2]. The advantages of these systems over batteries are indeed their higher power density, much longer cycle-life and faster charging-discharging times. However, since the charge is stored electrostatically by adsorbing the ions from the electrolytic solution on the surface of the active material by charging the so-called double layer, the specific energy of supercapacitors is nearly 1 order of magnitude lower than in batteries (about 10 vs. 100 Wh kg^{-1}, respectively) where the charge storing mechanism involves bulk faradic or redox reactions [3].

Material wise, the most widely used supercapacitors are those based on highly conductive, high surface area carbon materials [4–6]. The specific energy of these materials, ranging from activated carbons to the more in demand graphene [7, 8], can be increased when using organic electrolytes or ionic liquids instead of aqueous electrolytes, i.e., when enlarging the cell potential. A second type of materials comprises conducting polymers and metal oxides, in which the main charge storage mechanism is associated with fast and reversible surface faradic reactions, although double layer capacitance contribution can also play a minor role in the total charge storage capability. Consequently, these materials, also referred as pseudocapacitive materials,

can exhibit higher capacitance and, ultimately, higher specific energy than the carbon counterparts in a given electrolyte [9].

Among the major requirements that a metal oxide should fulfill in supercapacitor applications, high electrical conductivity and accessible oxidation states over a range of potentials with no irreversible transformations are of great importance. Regarding these properties and the resulting electrochemical performance, RuO_2 still seems to be the best choice [10], with capacitance values that in the case of amorphous $RuO_2{\cdot}nH_2O$ can reach about 900 F g^{-1} in a potential window of 0.8 V [11]. However, the high cost of ruthenium limits the use of its oxides to military, spatial or medical applications where the budget is not an issue. In the search of a synergy among cost, safety and electrochemical performance, MnO_2 polymorphs have turned out to be good candidates [12–14], among which the layered birnessite has emerged as a good compromise between electrochemical performance and sample preparation. In any case, hindered by its poor conductivity and with the only exception of very thin layers of material [15], the specific capacitance of MnO_2 is far from the theoretical 1,250 F g^{-1}, calculated for a redox process involving one electron per manganese atom in a potential window of 0.9 V, and instead it rarely exceeds 400 F g^{-1} [16–20]. The large fluctuations in specific capacitance values that can be found in the literature come principally from the very diverse synthetic routes followed by each research group, which affect the chemical composition, crystallinity, morphology and particle size, and eventually the pseudocapacitive behavior.

In this sense, we have chosen the decomposition of an organometallic precursor in a polyalcohol medium at mild temperature as the method to synthesize birnessite-type nanostructured MnO_2. This so-called polyol method is considered one of the most facile and efficient methods to synthesize nanosized materials. It has already been successfully used to prepare various metal oxide nanoparticles [21–24] and nanosized $LiFePO_4$ for Li-ion battery applications [25, 26]. Regarding manganese oxides, Mn_2O_3 and Mn_3O_4 nanoplates of different shapes [27] and 5–13 nm size nanocrystals of Mn_3O_4 for catalytic [28] or magnetic [29] applications have been synthesized. However, as far as we are concerned, no MnO_2 has been prepared following this synthetic route.

Herein, we present a novel method to obtain nanostructured MnO_2 with birnessite-type structure via the polyol method. The material was studied as a possible candidate for aqueous supercapacitor electrodes both in a conventional three-electrode cell and also by means of cavity microelectrode (CME) technique. Electrochemical tests were performed both in the conventional potential window of 0.8 V and also in a larger potential window of 1.9 V to evaluate the potential usage of the material for high current applications.

Experimental

Materials

Manganese(II) acetylacetonate (Mn(acac)2) and triethylene glycol (TREG) (≥99 %) were purchased from Sigma-Aldrich and used as received without further purification. Sodium hydroxide (98.9 %) was from Fisher Scientific, ethanol and acetone were purchased from Panreac S.A., whereas super 65 conductive black additive was from TimCal.

Synthesis of nanostructured MnO_2

Nanostructured MnO_2 was prepared by reducing Mn(acac)2 in a polyol medium according to a modification of previously reported protocols [23, 30]. $Mn(acac)_2$ (2 mmol) was dispersed in triethylene glycol (30 mL) and stirred at room temperature (18 °C) under a flow of N_2 for 30 min. Under continuously stirring (150 rpm), the mixture was first heated at 180 °C for 30 min and then heated to reflux (∼260 °C) for another 30 min. Subsequently, the heating of the mixture was stopped and the black-brown mixture was cooled down to room temperature (∼2 h). Under ambient conditions, a 50:50 mixture of ethanol and deionized water was added to the organic mixture (∼50 mL) along with a lower volume of an aqueous NaOH solution (1 M, 1 mL). The whole mixture was first stirred for ∼1 min and later centrifuged (3,500 rpm, 10 min) to precipitate and separate a dark solid. The collected sample was redispersed in the ethanol–deionized water mixture and precipitated two more times by adding aqueous NaOH to the previous mixture. Finally, the basic mixture was repeatedly washed with acetone until pH ∼7, and after removing the solvent by centrifugation (3,500 rpm, 10 min), the final solid product was isolated. The so-obtained nanostructured MnO_2 dark solid could be redispersed in water or in ethanol.

Characterization

Thermogravimetric/differential thermal analysis (TGA) was performed in a Netzsch STA 449 F3 analyzer with a heating rate of 10 °C min^{-1} in Ar atmosphere. Fourier transform infrared (FTIR) spectrum was obtained with a Perkin Elmer Spectrum 400 FT-IR/FT-FIR spectrometer. Analytical measurements were carried out in an atomic emission spectrophotometer with inductively coupled plasma (ICP-AES) (Horiba Jobin Yvon, Activa) using a quartz Meinhard concentric nebulizer, a Scott-type spray

chamber and a standard quartz sheath connection between the spray chamber and the torch. Transmission electron microscopy (TEM) images were obtained using a FEI Tecnai G2 microscope at an acceleration voltage of 200 kV. Samples were prepared by drop-casting previously ethanol dispersed powders onto a copper grid. The crystallinity was analyzed by X-ray diffraction (XRD) using a Bruker D8 ADVANCE.

Electrochemical characterization

The electrochemical tests of the nanostructured MnO_2 were carried out with a BioLogic VMP3 or a SP-200 (for ultra-low current) Potentiostat/Galvanostats in a three-electrode configuration using two different working electrodes: a CME and a circular 1.5 cm^2 electrode, both in 0.1 M K_2SO_4 (aq) at 25 °C.

CME technique was used to study the electrochemical performance of the nanostructured MnO_2 powder at different scan rates, starting from 0.1 mV s^{-1} and going up to 1 V s^{-1}. One of the strong points of using the CME technique lays indeed in the ability to go up to several V s^{-1} due to the very low amount of active material studied in the cavity (ohmic drop arising from the bulk of the electrolyte can be neglected). The CME used in this study has already been described in a previous study [31]. Briefly, a hole of 30 μm in diameter and 40 μm in depth was produced by a laser beam at the end of a Pt wire of 60 μm in diameter sealed in a 50 mm thick glass wire. Inside the glass support, the Pt wire was connected to a Cu wire collector via the addition of carbon graphite powder.

For the sake of an optimal electrical contact, nanostructured MnO_2 powder was mixed with acetylene black in the 70/30 weight ratio. This dry composite was further milled in a mortar and manually pressed into the cavity. The so-prepared electrode was integrated to the electrochemical cell along with a Pt electrode (0.25 mm^2 plate) used as counter electrode and a Ag/AgCl (sat KCl) or, in the case of low scan rates, a Hg/Hg_2SO_4 (sat K_2SO_4) as reference electrode.

The electrochemical cell used in the three-electrode system comprised an activated carbon counter electrode, an Ag/AgCl (sat KCl) as a reference electrode and a MnO_2 composite electrode as the working electrode. 1.5 cm^2 circular working electrodes were prepared by mixing nanostructured MnO_2 powder, acetylene black and PTFE in the 60/30/10 weight ratio in the presence of ethanol. Like in the previous method, carbon black additive is required to improve the poor electronic conductivity of the manganese oxide. The mixture was continuously stirred until the evaporation of the solvent and the resulting black paste was subsequently rolled into films. After drying at 120 °C under vacuum, the ~190 μm thick films were cut into 1.5 cm^2 circular electrodes. Activated carbon electrodes were prepared using the same technique but mixing the active carbon (Norit DLC Super 30) with PTFE in the 95/5 weight ratio. The thickness of the so-prepared 1.5 cm^2 circular electrodes was ~200 μm.

The specific capacitance, C (F g^{-1}) of the MnO_2 composite electrode was determined by integrating the cyclic voltammogram to obtain the corresponding voltammetric charge, Q, and by dividing the latter by the weight of the active material in the composite electrode ($0.6m_{electrode}$) and by the width of the potential window (ΔE).

$$C = \frac{Q}{\Delta E \times 0.6m_{electrode}} \quad (1)$$

For the calculation, the voltammetric charge due to the presence of acetylene black (12 F g^{-1}) was subtracted from the Q value.

Results and discussion

Structural characterization

The XRD pattern of the sample synthesized using the polyol process and presented in Fig. 1 shows very broad diffraction maxima as expected for particle sizes within the nano domain. The peaks at 2θ values of 12.9°, 28.5°, 36.9° and 65.5° can be indexed as the layered 2D allotropic form of MnO_2 (birnessite) [13] (JCPDS 43-1456) with an average basal spacing of 6.8 Å. This interlayer distance depends strongly on the cationic (Na^+ or K^+) and H_2O content between the MnO_6 octahedra sheets. Thus, even if most of the synthetic process took place under nitrogen atmosphere and using organic solvents, the last step with NaOH (aq), which comprises solvent exchange and removal of TREG coating, seems to be crucial for the formation of the MnO_2 layered phase.

The presence of Na in the MnO_2 structure was confirmed by ICP-AES. The calculated ratio between Na and Mn (Na:Mn) was found to be 0.32:1, which also agrees with the layered birnessite structure [32]. TGA result shows a total weight loss of 18 % until about 500 °C that corresponds, first, to the evaporation of adsorbed water molecules (14 %, until 300 °C) and then to the loss of structural water (another 4 %) (Fig. 1b). Taking into account the Na content, the calculated ratio between structural H_2O and Mn (H_2O:Mn) was 0.26:1, that is, the final ratio among Na, H_2O and Mn was found to be 0.32:0.26:1. Above 500 °C, a third weight loss of 4.4 % occurs, most probably caused by the oxygen release

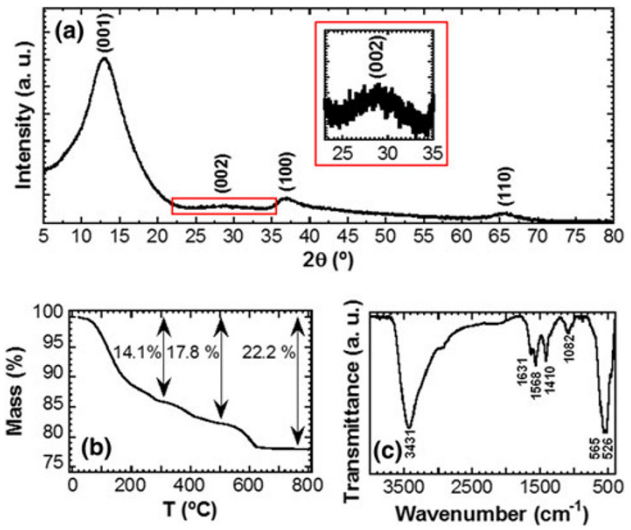

Fig. 1 **a** XRD pattern of the nanostructured MnO_2 synthesized by the thermal decomposition of $Mn(acac)_2$ along with the **b** FTIR spectra and **c** TGA measurement of the same sample

during the partial reduction of Mn(IV) as also reported for similar type of compounds [33]. Overall, the results suggest that the formula of our compound is $Na_{0.32}MnO_2{\cdot}0.26\ H_2O$ and the average oxidation state of Mn is 3.68.

The FTIR spectrum of the synthesized phase is shown in Fig. 1c. The broad and intense bands at 3,341 cm^{-1} and the sharper one at 1,631 cm^{-1} are characteristic of the stretching and bending modes of water and hydroxyl groups, respectively. These bands along with those appearing between 900 and 1,600 cm^{-1} and associated with different vibration modes of Mn with –OH, O and H^+ groups corroborate the presence of hydronium cations in the structure. The intense doublet at 565 and 526 cm^{-1} is characteristic of tetravalent manganese oxides with birnessite structure and corresponds to the Mn–O stretching vibrations [34, 35].

Figure 2 shows TEM images of the synthesized nanostructured MnO_2 along with the electron diffraction pattern. Contrary to the well-defined and dispersed nanoparticles usually obtained by the polyol method, herein the sample is made of agglomerated small particles of 3–5 nm packed in ~50 nm size clusters. Due to the high degree of agglomeration of the particles, it is difficult to give a more accurate size distribution. The nanoparticles display a platelet-type morphology which is in good accordance with the proposed 2D structure of the sample. Moreover, the structure rapidly decomposes and undergoes a phase transition under the electron beam due to the rapid evaporation of the H_2O molecules located in the interlayer of the MnO_6 octahedra sheets that hold the structure (Fig. 2a, b, d).

Electrochemical characterization

Conventional three-electrode cell

Figure 3a presents the cyclic voltammetry (CV) curve of the MnO_2 composite (MnO_2:acetylene black:PTFE) in 0.1 M K_2SO_4 (aq) using a three-electrode cell configuration with a 1.5 cm^2 working electrode. The CV displays almost a rectangular shape and a fast current response on potential reversal indicative of the pseudocapacitive nature of the sample. Note that the depicted curve is already the 20th one recorded and that the shape and the current were kept constant after the 2nd cycle. Very weak and broad oxidative and reductive peaks can also be observed at 0.6 and 0.4 V (vs. SHE) respectively, which could be due to a partial K^+ intercalation and deintercalation upon charge and discharge [36]. This cation diffusion seems to be favored by the layered structure of MnO_2. The calculated specific capacitance at 2 mV s^{-1} is 130 F g^{-1}, which is within the usual capacitance value range found in the literature for similar type of samples [19].

When the whole available potential window was explored, that is, from the overpotential for O_2 evolution (1.1 V vs. SHE) to the overpotential for H_2 evolution (−0.8 V vs. SHE), an intense reduction peak was observed at low potential values (−0.10 V vs. SHE) which corresponds to the dissolution of MnO_2 due to the Mn(IV) → Mn(II) reaction (Fig. 3b). At low scan rates, very few of the Mn(II) is retrieved again into the electrode, as indicated by the low intense and broad oxidative peak at 0.3 V (vs. SHE). Both Mn(IV) ↔ Mn(II) reactions start at ~0.1 V (vs. SHE) which is in good agreement with the potential value obtained in the Mn Pourbaix diagram for a solution of pH 7.06 like that of a 0.1 M K_2SO_4 (aq). As a result of this loss of material, the specific capacitance of MnO_2 is significantly reduced to almost half of the initial value of 177 mA h g^{-1} (335 F g^{-1}) only after one cycle and to 34 mA h g^{-1} (65 F g^{-1}) after 25 cycles (inset of Fig. 3b). Similar faradic processes, being almost 0.5 electron per unit formula reversible, had also been previously observed when using birnessite in alkaline electrolytes [37–39].

Cavity microelectrode (CME)

The solubility of Mn(II) in the electrolytic solution is well known and has been reported elsewhere [40]. One way to avoid this non-desirable faradic reaction is to reduce the operational potential window, just as shown in Fig. 3. To gain insight into the intrinsic properties of the MnO_2, the oxide was also studied using a CME in the same three-electrode configuration. Thus, parallel to the work done using a conventional cell, the CVs of the nanostructured MnO_2 were first recorded between 0.1 and 1,000 mV s^{-1},

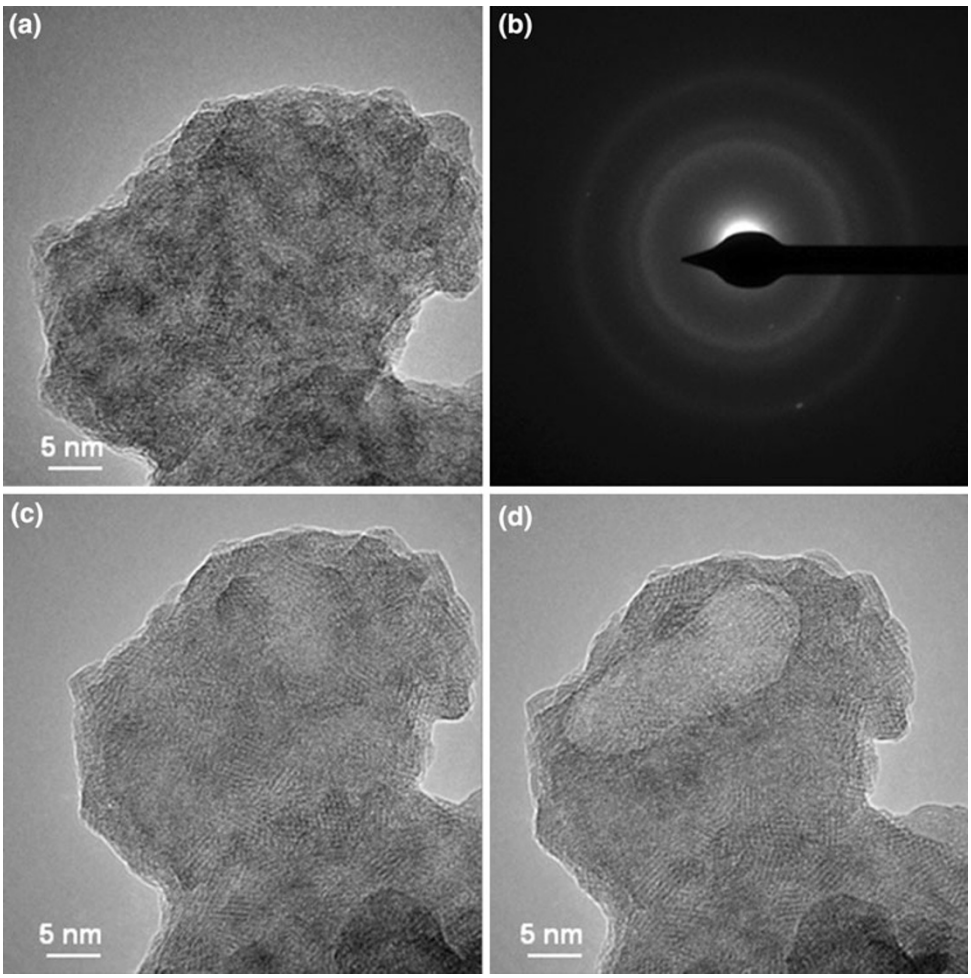

Fig. 2 **a** TEM image of the nanostructured MnO_2 synthesized using the polyol method. **b** The electron diffraction pattern of the sample. **c**, **d** TEM images of the sample after interacting with the electron beam

while the cell potential was controlled between 0.1 and 0.9 V (vs. SHE) using a CME cell. Figure 4a shows the CVs measured from 10 and up to 1,000 mV s^{-1} within the mentioned potential window. Note that the current intensity increases proportionally to the scan rate in the whole studied potential range following the $I = kv$ power law, where I is the current intensity in A at 0.5 V and v is the scan rate in V s^{-1} (Fig. 4b). Although slight distortions at high and low scan rates can be identified, in the full studied scan rate range, the curves show the typical rectangular shape as previously observed using conventional electrochemical cells (Fig. 3a). However, note that by CME and using very similar acetylene black to active material ratio, i.e., 30/70 in the conventional cell and 30/60 in the CME, the weak oxidative and reductive peaks observed at 0.6 and 0.4 V are no longer distinguished in all the studied scan rate range. At low scan rates (<10 mV s^{-1}), the plots slightly deviate from the ideal capacitive profile at about 0.1 V because the slower kinetics allow a faradic process to occur along with the redox pseudocapacitive charge storage. Besides, when going up to high scan rates (>200 mV s^{-1}), the CVs are also slightly distorted due to the increasing ohmic drop in the bulk electrolyte.

Owing to the good mechanical and electrochemical stabilities of the material within the 0.1–0.9 V (vs. SHE) potential window, all the previous CVs were obtained using the same batch of active material. However, for the subsequent electrochemical characterizations in a wider potential window (from −0.6 to 1.1 V vs. SHE) where the Mn dissolution in the electrolyte occurs in the form of Mn^{2+}, another procedure was followed. A different batch of active material was used for each of the scan rates and, after each measurement, the CME was washed and refilled again with the MnO_2–carbon black composite. The CME was also cycled at 100 mV s^{-1} in the 0.1–0.9 V (vs. SHE) potential range just before and after measuring any of the subsequent CVs. Although the precise mass inside the CME remained unknown, these reference cycles at 100 mV s^{-1} allowed us (1) to perform the normalization in mass of the CVs showing the faradic reactions (large potential window), (2) to estimate the standard deviation in the filling of the CME ($\sigma < 9.3$ %) and also (3) to evaluate the loss of material due the redox processes.

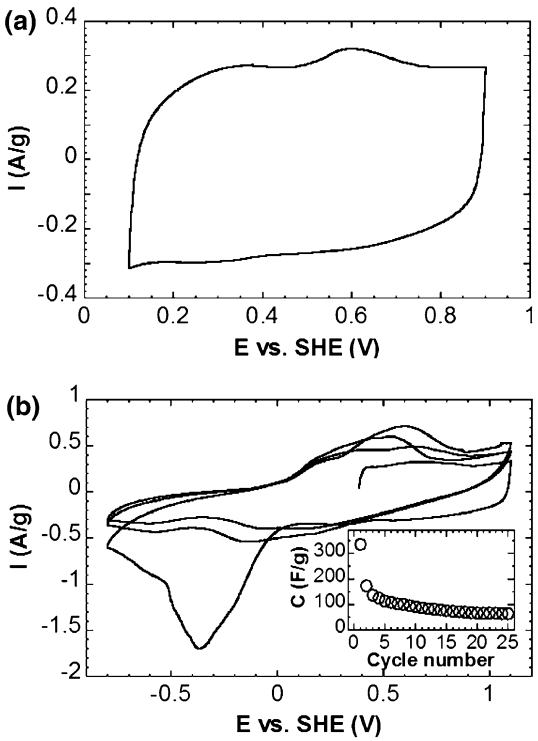

Fig. 3 CV curves of the nanostructured MnO_2 birnessite-type sample at 2 mV s^{-1} **a** in the 0.1–0.9 V vs. SHE potential window and **b** in the −0.8 to 1.1 V vs. SHE potential window. The *inset* shows the capacitance change in the large potential window after 25 cycles

Figure 4c shows the CVs obtained at different scan rates between −0.6 and 1.1 V (vs. SHE) after normalizing in mass following the procedure explained above. At intermediate scan rates such as 50 mV s^{-1}, the profile of the CV is similar to that depicted in Fig. 3b for the first cycle, that is, two current peaks can be well distinguished, one corresponding to the reduction of Mn(IV) to Mn(II) at −0.10 V (vs. SHE) and a second oxidative peak at 0.6 V (vs. SHE) corresponding to the oxidation reaction. However, as the scan rate increases, the CV becomes progressively more capacitive and already at 500 mV s^{-1} only a reduction peak can be observed at −0.20 V (vs. SHE). In this case, the peak intensities follow the linear law $I = kv^{1/2}$, which confirms their faradic nature (Fig. 4d).

This shape variation is highlighted while normalizing the CVs in current, which is performed by simply dividing the current by the scan rate just as shown in Fig. 5. This normalized CV profiles also emphasize the relation between peak separation (ΔE) and scan rate (v). Overall, from 0.5 to 200 mV s^{-1}, the peak separation increases almost logarithmically with increasing scan rate. At 0.5 mV s^{-1}, the peak separation is 480 mV, too large for a reversible system, and it increases about 150 mV every tenfold increase in v. Below 10 mV s^{-1}, the separation shift remains almost equal for both peaks, while just above 5 mV s^{-1} the shift in potential of the anodic peak is larger

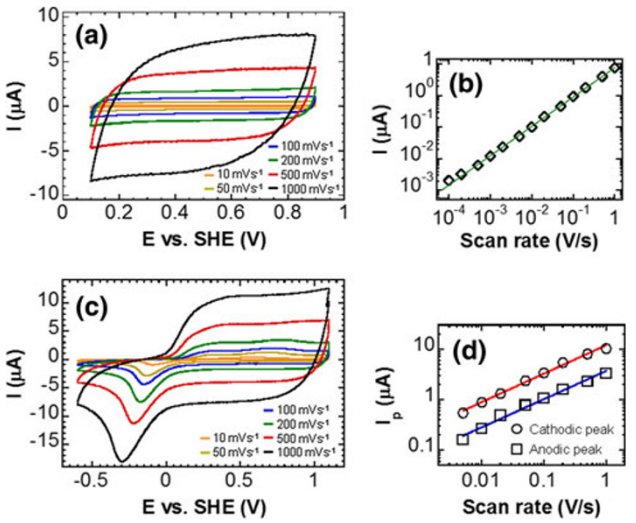

Fig. 4 **a** CV curves of the nanostructured MnO_2 birnessite-type sample at different scan rates in the 0.1–0.9 V vs. SHE potential window and **b** plot of the current intensity at 0.5 V as a function of the scan rate in a logarithm scale. **c** CV curves of the nanostructured MnO_2 birnessite-type sample at different scan rates in the −0.6 to 1.1 V vs. SHE potential window and **d** plot of the anodic (*white squares*) and cathodic (*white circles*) peak intensities as a function of the scan rate in a logarithm scale

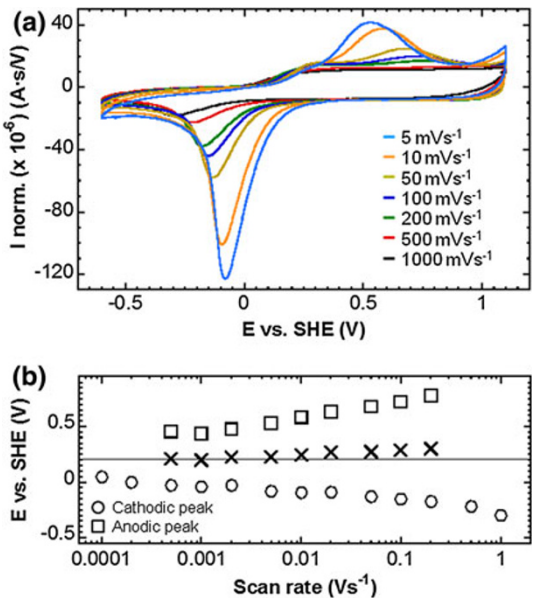

Fig. 5 **a** Normalized CV curves of the nanostructured MnO_2 birnessite-type sample at different scan rates in the −0.6 to 1.1 V vs. SHE potential window and **b** anodic (*white squares*) and cathodic (*white circles*) peak potential evolution at different scan rates. The *black crosses* show the mean peak potential

than that of the cathodic peak (40 mV larger every tenfold increase in v). At scan rates larger than 200 mV s^{-1} and lower than 0.5 mV s^{-1}, the oxidative peak diminishes and the peak separation cannot longer be studied.

For fast scan rates, the anodic peak is obscured by the capacitive envelope of the CV and the relative intensity of the reduction peak decreases about 10 times with respect to low scan rate CVs. In this scan rate regime, faradic reactions are hampered while capacitive processes are dominant which results in a low Mn dissolution. On the contrary, at low kinetics (<0.5 mV s^{-1}), Mn^{2+} cations generated in the cathodic process cannot be retrieved into the CME. Thus, the anodic peak corresponding to the Mn(II) → Mn(IV) reaction is no longer observed, but in this case, due to the undesired loss of active material. Although very recently specific capacitance values obtained by CME have been reported for MnO_2 [41], in general, CME technique does not allow performing precise quantitative measurements. In the present work, the active material loss was estimated from the discharge current fading. In this sense, while at 1,000 mV s^{-1} the discharge current remains almost constant from one cycle to the subsequent and, thus, the mass loss can be considered negligible (∼2 %), at 1 mV s^{-1} the current drops 25 % and already at 0.1 mV s^{-1} 84 %. Interestingly, this suggests that at high current rate, our nanoparticulate MnO_2 material can sustain an overvoltage with very small damage. This point could be really interesting for applications requiring high level of safety, which together with the high scan rate ability makes this compound a promising candidate for power applications. Note also that due to the good stability of the dispersions prepared in polar solvents such as water or ethanol (2–3 days), this nanostructured MnO_2 is well suited for thin electrode preparation. Overall, a particular effort should be made on the formulation of the nanostructured MnO_2 obtained by the polyol route for upscaling such compound for supercapacitor applications.

Conclusions

We report a simple and potentially scalable procedure to prepare nanostructured MnO_2 with birnessite-type layered structure starting from a polyol medium of Mn(acac)2 and followed by the reflux of the mixture in a two-step process first at 180 °C and finally at 260 °C under a flow of N_2. The layered structure of the oxide is kept stable thanks to the intercalated Na^+ and H_2O during the last stage of the synthetic process, which gives an average basal spacing of 6.8 Å. The sample consists of small platelet-type particles of 3–5 nm packed in ∼50 nm size clusters. When cycling the material at 2 mV s^{-1} in the usual potential window of 0.8–0.9 V, a capacitance value of 130 F g^{-1} was obtained, whereas in a larger potential window of 1.9 V, the initial capacitance was 335 F g^{-1} but faded to 65 F g^{-1} after 25 cycles due to the loss of active material through the reduction of Mn(IV) to the cationic state of Mn(II) at −0.10 V (vs. SHE). However, the reduced size of the particles offers shorter transport and diffusion path lengths for ions and electrons that can ultimately improve charge/discharge capacities at high current densities. CME technique allowed performing cycling tests from 0.1 up to 1,000 mV s^{-1} and showed that at high scan rates MnO_2 can be cycled without a significant Mn dissolution even within the largest potential window. These results along with the chemical and structural properties of the material open up the possibility of using the herein prepared nanostructured MnO_2 for high power requirement applications.

Acknowledgments The present work was supported by the Basque Government through Etortek project energiGUNE'10. The authors thank V. Roddatis (CIC Energigune) for TEM imaging, M. Casas-Cabanas (CIC Energigune) for her assistance with XRD measurements and SGIker Advanced Research Facilities from the University of the Basque Country for ICP-AES measurements.

References

1. Miller, J.R., Burke, A.F.: Electrochemical capacitors: challenges and opportunities for real-world applications. Electrochem. Soc. Interface **17**, 53–57 (2008)
2. Miller, J.R., Simon, P.: Electrochemical capacitors for energy management. Science **321**, 651–652 (2008)
3. Simon, P., Gogotsi, Y.: Materials for electrochemical capacitors. Nat. Mater. **7**, 845–854 (2008)
4. Pandolfo, A.G., Hollenkamp, A.F.: Carbon properties and their role in supercapacitors. J. Power Sources **157**, 11–27 (2006)
5. Zhai, Y., Dou, Y., Zhao, D., Fulvio, P.F., Mayers, R.T., Dai, S.: Carbon materials for chemical capacitive energy storage. Adv. Mater. **23**, 4828–4850 (2011)
6. Presser, V., Heon, M., Gogotsi, Y.: Carbide-derived carbons—from porous networks to nanotubes and graphene. Adv. Funct. Mater. **21**, 810–833 (2011)
7. Miller, J.R., Outlaw, R.A., Holloway, B.C.: Graphene double-layer capacitor with ac line-filtering performance. Science **329**, 1637–1639 (2010)
8. Zhu, Y., Murali, S., Stoller, M.D., Ganesh, K.J., Cai, W., Ferreira, P.J., Pirkle, A., Wallace, R.M., Cychosz, K.A., Thommes, M., Su, D., Stach, E.A., Ruoff, R.S.: Carbon-based supercapacitors produced by activation of graphene. Science **332**, 1537–1541 (2011)
9. Wang, G., Zhang, L., Zhang, J.: A review of electrode materials for electrochemical supercapacitors. Chem. Soc. Rev. **41**, 797–828 (2012)
10. Hadzi-Jordanov, S., Angerstein-Kozlowska, H., Vukoviff, M., Conway, B.E.: Reversibility and growth behavior of surface oxide films at ruthenium electrodes. J. Electrochem. Soc. **125**, 1471–1480 (1978)
11. Long, J.W., Swider, K.E., Merzbacher, C.I., Rolison, D.R.: Voltammetric characterization of ruthenium oxide-based aerogels and other RuO_2 solids: the nature of capacitance in nanostructured materials. Langmuir **15**, 780–785 (1999)

12. Feng, Q., Kanohb, H., Ooi, K.: Manganese oxide porous crystals. J. Mater. Chem. **9**, 319–333 (1999)
13. Ghodbane, O., Pascal, J.-L., Favier, F.: Microstructural effects on charge-storage properties in MnO_2-based electrochemical supercapacitors. ACS Appl. Mater. Interfaces **1**, 1130–1139 (2009)
14. Ghodbane, O., Pascal, J.-L., Fraisse, B., Favier, F.: Structural in situ study of the thermal behavior of manganese dioxide materials: toward selected electrode materials for supercapacitors. ACS Appl. Mater. Interfaces **2**, 3493–3505 (2010)
15. Toupin, M., Brousse, T., Belanger, D.: Charge storage mechanism of MnO_2 electrode used in aqueous electrochemical capacitor. Chem. Mater. **16**, 3184–3190 (2004)
16. Lee, H.Y., Goodenough, J.B.: Supercapacitor behavior with KCl electrolyte. J. Solid State Chem. **144**, 220–223 (1999)
17. Toupin, M., Brousse, T., Bélanger, D.: Influence of microstucture on the charge storage properties of chemically synthesized manganese dioxide. Chem. Mater. **14**, 3946–3952 (2002)
18. Wang, Y., Yuan, A., Wang, X.: Pseudocapacitive behaviors of nanostructured manganese dioxide/carbon nanotubes composite electrodes in mild aqueous electrolytes: effects of electrolytes and current collectors. J. Solid State Electrochem. **12**, 1101–1107 (2008)
19. Bélanger, D., Brousse, T., Long, J.W.: Manganese oxides: battery materials make the leap to electrochemical capacitors. Electrochem. Soc. Interface **17**, 49–52 (2008)
20. Li, W., Liu, Q., Sun, Y., Sun, J., Zou, R., Li, G., Hu, X., Song, G., Ma, G., Yang, J., Chen, Z., Hu, J.: MnO_2 ultralong nanowires with better electrical conductivity and enhanced supercapacitor performances. J. Mater. Chem. **22**, 14864–14867 (2012)
21. Sun, S., Zeng, H.: Size-controlled synthesis of magnetite nanoparticles. J. Am. Chem. Soc. **124**, 8204–8205 (2002)
22. Feldmann, C.: Polyol-mediated synthesis of nanoscale functional materials. Adv. Funct. Mater. **13**, 101–107 (2003)
23. Sun, S., Zeng, H., Robinson, D.B., Raoux, S., Rice, P.M., Wang, S.X., Li, G.: Monodisperse MFe_2O_4 (M = Fe, Co, Mn) nanoparticles. J. Am. Chem. Soc. **126**, 273–279 (2004)
24. Salado, J., Insausti, M., Lezama, L., Gil de Muro, I., Goikolea, E., Rojo, T.: Preparation and characterization of monodisperse Fe_3O_4 nanoparticles: an electron magnetic resonance study. Chem. Mater. **23**, 2879–2885 (2011)
25. Kim, D.-H., Kim, J.: Synthesis of $LiFePO_4$ nanoparticles in polyol medium and their electrochemical properties. Electrochem Solid State Lett. **9**, A439–A442 (2006)
26. Oh, S.W., Huang, Z.-D., Zhang, B., Yu, Y., He, Y.-B., Kim, J.-K.: Low temperature synthesis of graphene-wrapped $LiFePO_4$ nanorod cathodes by polyol method. J. Mater. Chem. **22**, 17215–17221 (2012)
27. Liu, L., Yang, Z., Liang, H., Yang, H., Yang, Y.: Shape-controlled synthesis of manganese oxide nanoplates by a polyol-based precursor route. Mater. Lett. **64**, 891–893 (2010)
28. Rhadfi, T., Piquemal, J.-Y., Sicard, L., Herbst, F., Briot, E., Benedetti, M., Atlamsani, A.: Polyol-made Mn_3O_4 nanocrystals as efficient Fenton-like catalysts. Appl. Cat. A **386**, 132–139 (2010)
29. Sicard, L., Le Meins, J.-M., Méthivier, C., Herbst, F., Ammar, S.: Polyol synthesis and magnetic study of Mn_3O_4 nanocrystals of tunable size. J. Magn. Magn. Mater. **322**, 2634–2640 (2010)
30. Wan, J., Cai, W., Feng, J., Meng, X., Liu, E.: In situ decoration of carbon nanotubes with nearly monodisperse magnetite nanoparticles in liquid polyols. J. Mater. Chem. **17**, 1188–1192 (2007)
31. Come, J., Taberna, P.-L., Hamelet, S., Masquelier, C., Simon, P.: Electrochemical kinetic study of $LiFePO_4$ using cavity microelectrode. J. Electrochem. Soc. **158**, A1090–A1093 (2011)
32. Hu, Y., Zhu, H., Wang, J., Chen, Z.: Synthesis of layered birnessite type manganese oxide thin films on plastic substrates by chemical bath deposition for flexible transparent supercapacitors. J. Alloys Comp. **509**, 10234–10240 (2011)
33. Yang, X., Makita, Y., Liu, Z.-H., Sakane, K., Ooi, K.: Structural characterization of self-assembled MnO_2 nanosheets from birnessite manganese oxide single crystals. Chem. Mater. **16**, 5581–5588 (2004)
34. Potter, R.M., Rossman, G.R.: The tetravalent manganese oxides: identification, hydration, and structural relationships by infrared spectroscopy. Am. Miner. **64**, 1199–1218 (1979)
35. Anant, M.V., Pethkar, S., Dakshinamurthi, K.: Distortion of MnO_6 octahedra and electrochemical activity of Nstutite-based MnO_2 polymorphs for alkaline electrolytes-an FTIR study. J. Power Sources **75**, 278–282 (1998)
36. Brousse, T., Toupin, M., Dugas, R., Athouël, L., Crosnier, O., Bélanger, D.: Crystalline MnO_2 as possible alternatives to amorphous compounds in electrochemical supercapacitors. J. Electrochem. Soc. **153**, A2171–A2180 (2006)
37. Donne, S.W., Lawrance, G.A., Swinkels, D.A.J.: Redox processes at the manganese dioxide electrode.1. Constant-current intermittent discharge. J. Electrochem. Soc. **144**, 2949–2953 (1997)
38. Donne, S.W., Lawrance, G.A., Swinkels, D.A.J.: Redox processes at the manganese dioxide electrode 2. Slow-scan cyclic voltammetry. J. Electrochem. Soc. **144**, 2954–2961 (1997)
39. Donne, S.W., Lawrance, G.A., Swinkels, D.A.J.: Redox processes at the manganese dioxide electrode 3. Detection of soluble and solid intermediates during reduction. J. Electrochem. Soc. **144**, 2961–2967 (1997)
40. Raymundo-Piñero, E., Khomenko, V., Frackowiak, E., Béguin, F.: Performance of manganese oxide/CNTs composites as electrode materials for electrochemical capacitors. J. Electrochem. Soc. **152**, A229–A235 (2005)
41. Athouël, L., Arcidiacono, P., Ramirez-Castro, C., Crosnier, O., Hamel, C., Dandeville, Y., Guillemet, P., Scudeller, Y., Guay, D., Bélanger, D., Brousse, T.: Investigation of cavity microelectrode technique for electrochemical study with manganese dioxides. Electrochim. Acta **86**, 268–276 (2012)